21st Australasian Fluid Mechanics Conference
Adelaide, Australia
10-13 December 2018

Numerical Investigation of Secondary Flows in a Turbulent Pipe Flow with Sinusoidal Roughness

L. Chan, M. MacDonald, D. Chung, N. Hutchins and A. Ooi

Department of Mechanical Engineering
The University of Melbourne, Victoria 3010, Australia

Abstract

Recent research on turbulent flow over heterogeneous rough walls have reported the occurrence of secondary motions which extend to the edge of the boundary layer. In this study, direct numerical simulations (DNSs) of turbulent flow in a rough-wall pipe are conducted where the pipe surface consists of a three-dimensional sinusoidal surface. The roughness semi-amplitude height (h^+) is fixed at 60 viscous units while the wavelength of the roughness elements is varied to investigate the effects of solidity or effective slope (ES). The rough-wall cases, which vary from the wavy regime ($ES = 0.18$ with a viscous roughness wavelength, λ^+ of 848) to the closely packed roughness/dense regime ($ES = 0.72$, $\lambda^+ = 212$), have a staggered arrangement. Using the triple decomposition, the time-independent dispersive stresses, which arise due to the stationary features of the flow, are found to increase in magnitude with roughness wavelength. These dispersive stresses, which are maximum in the roughness canopy, are due to the occurrence of secondary flows. These secondary flows transport high-speed fluid from the outer region to the near-wall region and pump low-speed fluid from the near-wall region to the outer region. For the range of cases simulated here, the wall-normal and spanwise extent of these secondary motions are found to scale with the roughness spanwise wavelength. This gives an indication of how the roughness sublayer is related to the degree of surface heterogeneity, with spanwise homogeneous flow only observed once the distance from the wall exceeds the spanwise spacing of the roughness. For the case with the largest wavelength ($ES = 0.18$), the secondary flows occupy a significant portion of the pipe cross-section.

Introduction

There have been a spark of interest in the occurrence of secondary flows in wall-bounded turbulent flows over heterogeneous roughness in recent years, particularly due to the papers by [14] and [2]. They found that the turbulent flow over their highly irregular test surface (a damaged turbine blade due to the deposition of foreign material) resulted in alternating regions of low and high momentum (known as high momentum paths (HMPs) and low momentum paths (LMPs)). This caused the occurrence of secondary flows which disrupt the near-wall cycle.

It is generally agreed that the spanwise variation of the skin-friction velocity U_τ ($\equiv \sqrt{\tau_w/\rho}$, where τ_w is the wall-shear stress and ρ is density) whether due to spatial variations in the roughness characteristics or as modelled in numerical simulations, induces secondary flows [18, 1, 13, 5]. These secondary flows are stress-induced and are categorised as Prandtl's secondary flow of the second kind [18, 1].

Experimental and numerical studies have been conducted where the spanwise wavelength of the roughness l_s is systematically altered [19, 17, 13, 5]. These studies, which have streamwise aligned roughness, have shown that the size of the secondary flows increases with increasing roughness spanwise length and are prominent when the spanwise spacing of the roughness is approximately equal to the boundary layer thickness δ. [19] defined three regimes based on the spanwise spacing of the roughness. The surface is considered a topography when $l_s/\delta \gtrsim 2$ and the surface behaves as a homogeneous roughness when $l_s/\delta \lesssim 0.2$. For $0.2 \lesssim l_s/\delta \lesssim 2$, the surface is in the intermediate regime where secondary flows exist. Indeed the spanwise length scale of the roughness heterogeneity to the boundary layer thickness is a critical parameter in determining the occurrence of large secondary flows which disrupt the near-wall cycle of the boundary layer. From dimensional analysis, it can be shown that the ratio l_s/δ must be small ($l_s << \delta$) for a global outer-layer similarity to be observed [5].

In this paper, a systematic study has been carried out where the wavelength of the roughness in a pipe is altered while maintaining a fixed roughness height. The sinusoidal roughness ranges from a wavy undulating surface to a closely packed egg-carton type roughness. Though this surface would typically be classified as homogeneous, the cases with low ES exhibit spatial variations of the roughness height which will begin to exhibit heterogeneous-type behaviour.

Computational Setup

The incompressible Navier–Stokes equation was solved without turbulence modelling using CDP which is a second-order, energy-conserving finite-volume code. The rough-wall pipe has a Cartesian 'O-grid' mesh which conforms to the three-dimensional sinusoidal roughness elements. Figure 1 shows a sketch of the computational domain and highlights some of the characteristics of the roughness. A periodic boundary condition is applied to the ends of the pipe and the no-slip impermeable boundary condition is used for the pipe's surface. The turbulent flow is simulated at a friction Reynolds number of $Re_\tau = 540$ (where $Re_\tau = R_0 U_\tau/\nu$, R_0 is the mean/reference radius of the pipe, U_τ is the time-space averaged friction velocity, and ν is the kinematic viscosity). x, r and θ are the streamwise, radial and azimuthal directions. y is the wall-normal direction where the virtual origin is set to be located at the mean/reference radius of the pipe ($y^+ = 0$ at R_0). Further details of the numerical method used can be found in [3].

Throughout the paper, the roughness cases are identified by the following identifying code

$$\underbrace{\boxed{6}\boxed{0}}_{h^+}\text{-}\underbrace{\boxed{4}\boxed{2}\boxed{4}}_{\lambda^+} \qquad (1)$$

where the first two digits represent the roughness semi-amplitude height and the last three digits represent the streamwise or spanwise wavelength of the roughness elements ($\lambda_x = \lambda_s$). The computational details and mean flow properties of the rough cases are tabulated in table 1.

Second-order Statistics

To analyse the turbulent flow over roughness, the triple decomposition is applied to the turbulent quantity where it is decom-

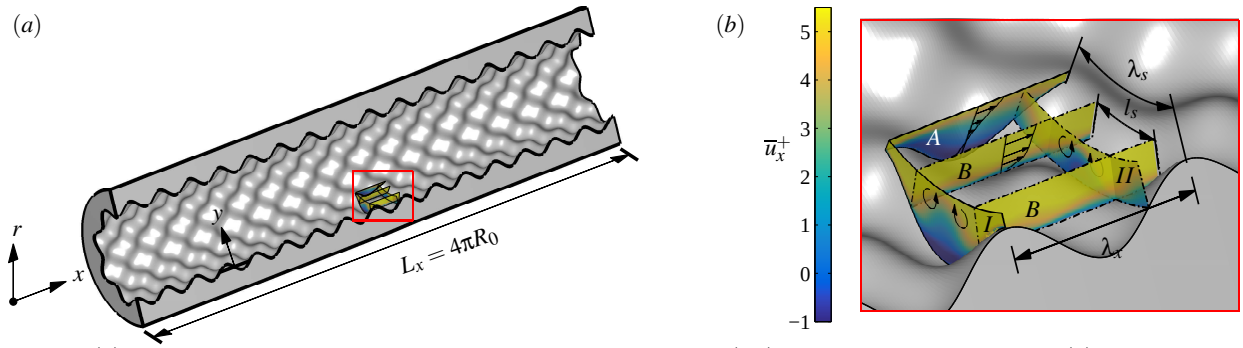

Figure 1: (a) Sketch of the roughness case 60_424 with an effective slope (ES) of 0.36. Close up sketch in (b) illustrates contour of the time-averaged streamwise velocity. Cross-sectional plane I and streamwise plane A are the planes which are locally rough and cross-sectional plane II and streamwise plane B are the planes which are locally smooth λ_x and λ_s are the roughness streamwise and spanwise wavelengths and l_s is the roughness spanwise spacing corresponding to half of λ_s due to the staggered arrangement of the roughness.

Case	Symbol	$N_{r,\theta}$	N_x	N_{λ_x}	Δr^+	Δx^+	k_a^+	ES	Re_D	ΔU^+
Smooth	○	94752	1152	-	0.23	5.0	0	0	18792	-
60_848	△	109440	1152	144	0.15	4.4	24.3	0.18	9602	9.43
60_424	△	108720	1152	72	0.15	4.0	24.3	0.36	7871	10.44
60_283	△	109440	1152	48	0.09	3.9	24.3	0.54	7305	10.42
60_212	△	109440	1152	36	0.08	3.5	24.3	0.72	7622	10.38

Table 1: Details of the computational mesh and mean flow properties of the cases simulated. $N_{r,\theta}$ is the number of elements in an (r,θ) plane, N_x the number of elements in the streamwise direction and N_{λ_x} the number of elements per roughness wavelength. Δr^+ and Δx^+ are the radial and streamwise mean viscous grid spacings at the wall calculated using the local time-averaged friction velocity $\overline{u}_\tau$. The largest cells are located at the centre of the pipe where $\Delta r^+ \approx \Delta r\theta^+ \approx \Delta x^+$. k_a^+ is the average roughness height and ES is the effective slope of the roughness (see [3]). $Re_D = 2R_0U_b/\nu$ is the bulk Reynolds number where U_b is the bulk velocity and ΔU^+ is the Hama roughness function.

posed into three components [16, 6],

$$u_i = U_i + \tilde{u}_i + u_i''. \tag{2}$$

Here, $U_i = \langle\overline{u_i}\rangle$ is the spatial and temporal averaged mean, which is also known as the global mean and $\tilde{u}_i = \overline{u}_i - U_i$ is the spatial variation of the time-averaged flow around individual roughness elements (also known as the coherent or dispersive component). u_i'' is the turbulent fluctuation. For a smooth wall, $\tilde{u}_i = 0$ and therefore $U_i = \overline{u_i}$. The triple decomposition is a result from double averaging, where the governing equations are averaged over time and then in space. This technique has been used to analyse plant canopy flows (urban-canopy model) [15, 7, 8] and also in numerical simulations of turbulent flows over roughness [9, 4, 10].

Figure 2 shows the root-mean-squared (rms) of the turbulent fluctuation and also the coherent fluctuation of the streamwise velocity. Good collapse with the smooth wall profile in the outer region is observed for the streamwise velocity turbulent fluctuation stress. The coherent fluctuations increases significantly with increasing roughness wavelength. The streamwise velocity coherent stress is dominant within the roughness canopy but drops to zero above the crest of the roughness at wall-normal heights proportional to the wavelength of the roughness. For case 60_848, the coherent stress extends up to $y^+ \approx 300$ (more than half of the boundary layer thickness) indicating large time-independent fluctuating motions in the flow due to the roughness.

In figure 3, the coherent stress is plotted against wall-normal height normalised by the roughness wavelength. It appears that the coherent stresses, which is commonly interpreted as the roughness sublayer, reduced to zero at wall-normal heights above half of the roughness wavelength. Cases 60_212 and 60_283, which have large ES values, do not collapse well onto the other rough wall profiles because the actual virtual origin for these cases have shifted ($y^+ \neq 0$ at R_0). It is expected that the virtual origin of the rough surface resides closer to the crest of the roughness with increasing ES as it asymptotes to a smooth wall with the virtual origin shifted to the crest of the roughness [12]. Correcting the wall-normal location by setting the virtual origin to be the location where $U^+ = 2$ in the inset of figure 3, a more convincing collapse in the profiles are observed.

Streamwise Velocity Contours

The time-averaged streamwise velocity contour overlaid with the line contour of the time-averaged streamwise vorticity is illustrated in figure 4. The time-averaged streamwise vorticity shows the occurrence of counter rotating secondary flows which predominantly occurs within the roughness canopy. As the roughness wavelength increases, these secondary flows become larger both in the spanwise and wall-normal direction. The effects of the secondary flows are noticeable from the azimuthal variation of the time-averaged streamwise velocity contours, especially for case 60_848. We observe that high-speed fluid is transported from the outer-region to the inner region along streamwise planes which are locally smooth (plane B) and conversely low-speed fluid is ejected to the outer-region of the flow along streamwise planes which are locally rough (plane A). These are contrary to the high- and low-momentum paths (HMP and LMP) observed by [14] which occurred along the rough and smooth regions respectively.

Kevin et al. [11], who conducted experiments on directional riblets also reported the observation of large albeit weak secondary flows. They concluded that these secondary flows in the time-averaged velocity field are not persistent at all instantaneous times and might be an artefact arising from superpositions of much stronger instantaneous turbulent events enhanced

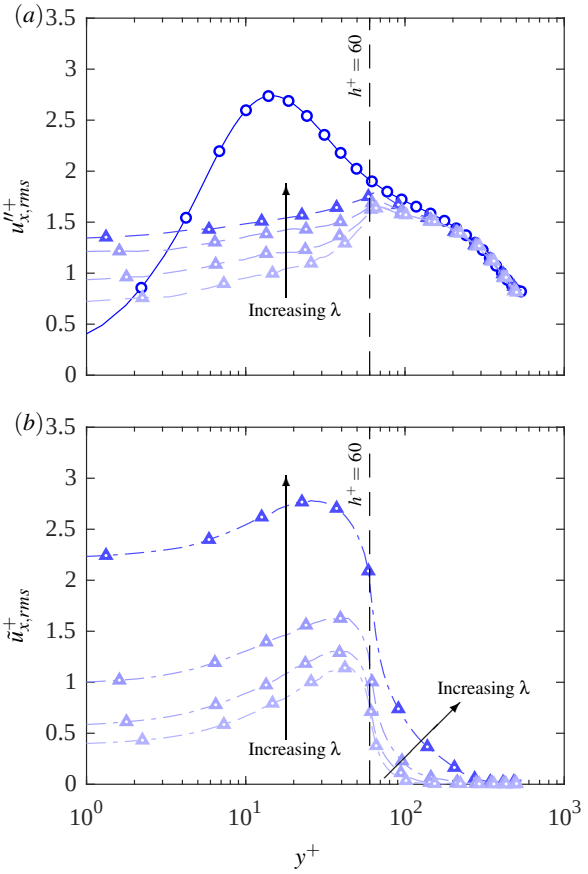

Figure 2: Streamwise velocity stress due to (a) turbulent fluctuation $u''^+_{x,rms}$ and (b) coherent fluctuation $\tilde{u}^+_{x,rms}$.

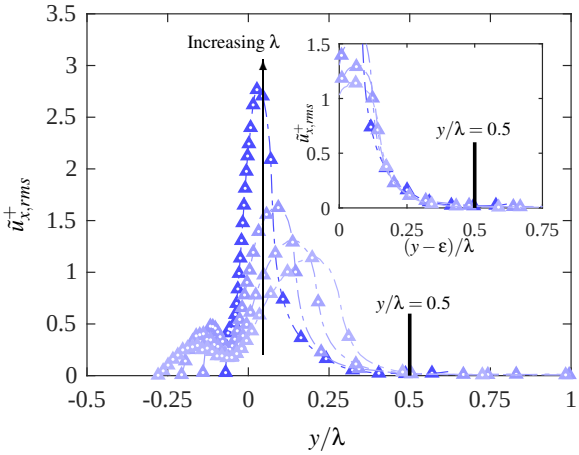

Figure 3: Streamwise velocity stress due to coherent fluctuation. The wall-normal height of the profiles are normalised by the roughness wavelength with the inset profile adjusted to take into account the location of the corrected virtual origin offset ε (defined as the location where $U^+ = 2$).

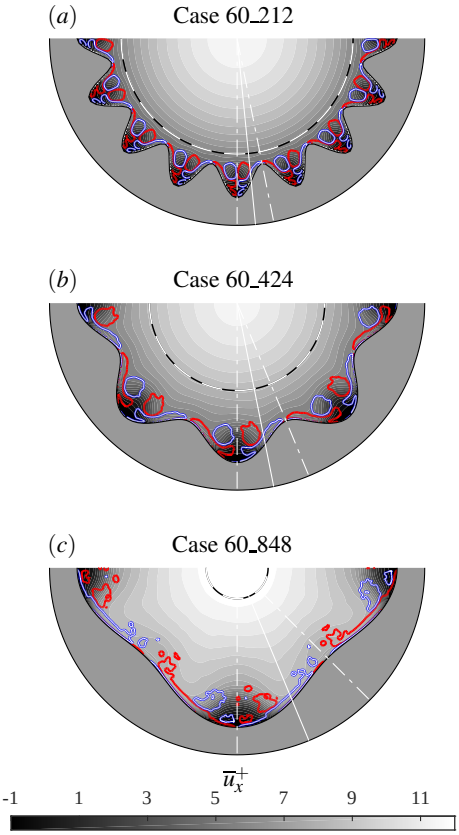

Figure 4: Contours of the time-averaged streamwise velocity $\overline{u}^+_x$ overlaid with line contours of $\overline{\omega}^+_x = +0.01$ (red line) and $\overline{\omega}^+_x = -0.01$ (blue line) along plane I where the cross-section of the pipe is locally rough. The dashed black and white lines are at $y/\lambda = 0.5$ where the coherent stresses are zero. White dashed-dotted and solid lines represents streamwise plane A (rough) and B (smooth) respectively. Flow is into the page.

by the riblets. A similar analysis has been conducted here to investigate the persistence of the secondary motions. Conditional averaging on 832 independent instances was conducted to determine the probability of the occurrence of downward flows towards the walls along plane B (HMP) and upward flows from the wall along plane A (LMP). The instantaneous wall-normal velocity is averaged in window between $100 < y^+ < 200$ and a width of 0.064λ at every quarter of the roughness wavelength (at LMPs and HMPs). The results in figure 5 show that this flow configuration only occurs $\approx 18.5\%$ and $\approx 20.3\%$ of the instances along plane I and plane II respectively compared to $\approx 13\%$ in an equivalent smooth wall. This value is lower than the 27.8% reported by [11] for their converging-diverging riblets. Nevertheless, this analysis shows that the secondary motions observed in the time-averaged field are not an accurate representation of the vigorous turbulent events enhanced by the roughness which may occur in short time-scales.

Conclusions

DNS of a turbulent flow in a pipe with sinusoidal roughness is conducted where the roughness spans from the wavy/undulating roughness to the dense, closely packed roughness. The triple decomposition is used to separate the coherent (or dispersive) fluctuations due to the roughness elements, from the turbulent fluctuations. The wall-normal extent of the coherent fluctuations, which typically defines the roughness sublayer, is a clear function of the roughness spanwise wavelength. These coherent fluctuations are due to the occurrence of secondary motions when analysing the time-averaged velocity field. For the case with the largest wavelength, which resembles a wavy surface, the secondary flows occupy more than half of the pipe's boundary layer. The occurrence of secondary flows for this homogeneous type roughness is consistent with the findings in the literature for streamwise aligned heterogeneous roughness

[17, 18, 19, 13]. Conditional averaging for the instantaneous flow field shows that these time-averaged secondary motions are artefacts of much stronger instantaneous events that are enhanced by the spatial distribution of the roughness elements [11].

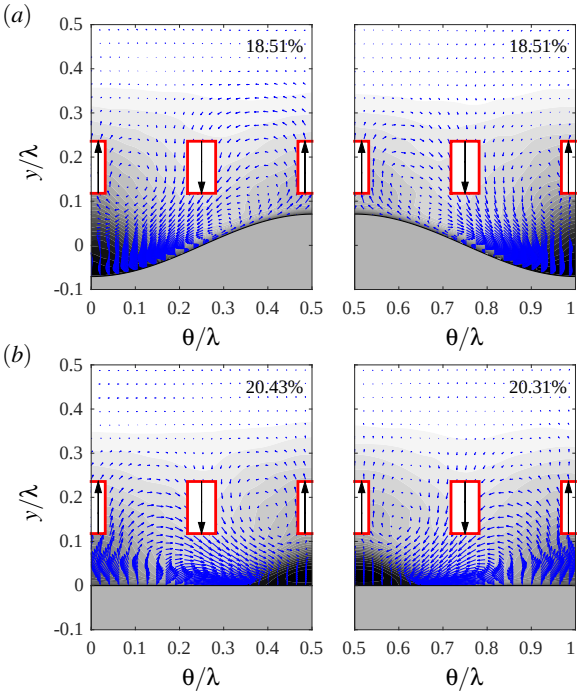

Figure 5: Conditional average of the streamwise velocity along the unwrapped cross-sectional (*a*) plane *I* (rough) and (*b*) plane *II* (smooth). The percentage represents the occurrence of this flow configuration. The red box illustrates the window ($0.118 < y/\lambda < 0.236$ and $\Delta\theta/\lambda = 0.064$) where the wall-normal velocity is averaged.

Acknowledgements

The authors would like to gratefully thank the Australian Research Council for the financial support and the Victorian Life Science Computational Institute (VLSCI) for providing the computational time.

References

[1] Anderson, W., Barros, J. M., Christensen, K. T. and Awasthi, A., Numerical and experimental study of mechanisms responsible for turbulent secondary flows in boundary layer flows over spanwise heterogeneous roughness, *J. Fluid Mech.*, **768**, 2015, 316–347.

[2] Barros, J. M. and Christensen, K. T., Observations of turbulent secondary flows in a rough-wall boundary layer, *J. Fluid Mech.*, **748**, 2014, R1.

[3] Chan, L., MacDonald, M., Chung, D., Hutchins, N. and Ooi, A., A systematic investigation of roughness height and wavelength in turbulent pipe flow in the transitionally rough regime, *J. Fluid Mech.*, **771**, 2015, 743–777.

[4] Chan, L., MacDonald, M., Chung, D., Hutchins, N. and Ooi, A., Secondary motion in turbulent pipe flow with three-dimensional roughness, *J. Fluid Mech.*, **854**, 2018, 5–33.

[5] Chung, D., Monty, J. P. and Hutchins, N., Similarity and structure of wall turbulence with lateral wall shear stress variations, *J. Fluid Mech.*, **847**, 2018, 591–613.

[6] Coceal, O. and Belcher, S. E., A canopy model of mean winds through urban areas, *Quart. J. Roy. Meteorol. Soc.*, **130**, 2004, 1349–1372.

[7] Finnigan, J. J., Turbulent transport in flexible plant canopies, in *The Forest-Atmosphere Interaction*, Springer, 1985, 443–480.

[8] Finnigan, J. J., Turbulence in plant canopies, *Annu. Rev. of Fluid Mech.*, **32**, 2000, 519–571.

[9] Jelly, T. O. and Busse, A., Impact of irregular anisotropic surface roughness on the near-wall region of turbulent channel flow, in *12th International ERCOFTAC Symposium on Engineering Turbulence Modelling and Measurements*, 2018.

[10] Jelly, T. O. and Busse, A., Reynolds and dispersive shear stress contributions above highly skewed roughness, *J. Fluid Mech.*, **852**, 2018, 710–724.

[11] Kevin, Monty, J. P., Bai, H. L., Pathikonda, G., Nugroho, B., Barros, J. M., Christensen, K. T. and Hutchins, N., Cross-stream stereoscopic particle image velocimetry of a modified turbulent boundary layer over directional surface pattern, *J. Fluid Mech.*, **813**, 2017, 412–435.

[12] MacDonald, M., Chan, L., Chung, D., Hutchins, N. and Ooi, A., Turbulent flow over transitionally rough surfaces with varying roughness densities, *J. Fluid Mech.*, **804**, 2016, 130–161.

[13] Medjnoun, T., Vanderwel, C. and Ganapathisubramani, B., Characteristics of turbulent boundary layers over smooth surfaces with spanwise heterogeneities, *J. Fluid Mech.*, **838**, 2018, 516–543.

[14] Mejia-Alvarez, R. and Christensen, K. T., Wall-parallel stereo particle-image velocimetry measurements in the roughness sublayer of turbulent flow overlying highly irregular roughness, *Phys. Fluids*, **25**, 2013, 115109.

[15] Raupach, M. R. and Shaw, R. H., Averaging procedures for flow within vegetation canopies, *Bound-Layer Meteor.*, **22**, 1982, 79–90.

[16] Reynolds, W. C. and Hussain, A. K. M. F., The mechanics of an organized wave in turbulent shear flow. Part 3. Theoretical models and comparisons with experiments, *J. Fluid Mech.*, **54**, 1972, 263–288.

[17] Vanderwel, C. and Ganapathisubramani, B., Effects of spanwise spacing on large-scale secondary flows in rough-wall turbulent boundary layers, *J. Fluid Mech.*, **774**, 2015, R2–1–R2–12.

[18] Willingham, D., Anderson, W., Christensen, K. T. and Barros, J. M., Turbulent boundary layer flow over transverse aerodynamic roughness transitions: Induced mixing and flow characterization, *Phys. Fluids*, **26**, 2014, 025111.

[19] Yang, J. and Anderson, W., Numerical study of turbulent channel flow over surfaces with variable spanwise heterogeneities: topographically-driven secondary flows affect outer-layer similarity of turbulent length scales, *Flow Turbul. Combust.*, **100**, 2018, 1–17.